Int. J. Heat Mass Transfer. Vol. 36, No. 4, pp. 931–940, 1993
Printed in Great Britain

0017–9310/93 $6.00 + 0.00
© 1993 Pergamon Press Ltd

Effect of ridge shapes on turbulent heat transfer and friction in a rectangular channel

TONG-MIIN LIOU and JENN-JIANG HWANG†
Department of Power Mechanical Engineering, National Tsing Hua University, Hsinchu, Taiwan 300, R.O.C.

(*Received* 2 *January* 1992 *and in final form* 29 *April* 1992)

Abstract—Turbulent heat transfer and friction in a channel with various-shaped ridges mounted on two opposite walls has been investigated experimentally. Experiments were conducted for three ridge shapes, namely triangular, semicircular, and square cross sections. The ridges are oriented transversely to the main stream in a periodic arrangement. The technique of real-time holographic interferometry is used to measure local and average heat transfer. The ridge pitch-to-height(radius) ratio varies from 8.0 to 20; the Reynolds number varies from 7800 to 50 000; and the ridge height(radius)-to-channel hydraulic diameter ratio is 0.08. The results show that the three types of ridged channels have comparable thermal performances. It is also noted that the semicircular and triangular ridge geometries are less likely to yield the hot-spots behind the ridges than the square one. Moreover, a comparison of the average heat transfer coefficient of the wall with thermally active ridges and that with thermally nonactive ridges is made. Compact correlations in terms of roughness parameters are developed for both the fully developed heat transfer coefficients and friction factors. The correlations can be used in the design of turbine blade cooling passages.

INTRODUCTION

IN THE modern turbine blade, heat transfer enhancement is accomplished by installing turbulence promoters, such as artificial roughness, on the two opposite walls of the internal cooling passages. Usually, the roughness elements are small ridges of a square cross section and are placed periodically at right angles to the main flow direction. The cost paid for the higher heat transfer is an increase in the pressure drop. Turbine airfoil cooling designers would like to optimize the ridge geometry in order to obtain the best heat transfer coefficients for either a given coolant flow rate or an available pressure drop across the cooling passage. The ability to predict analytically the effects of the ridge geometry on the flow field and heat transfer is limited. Therefore, many experimental investigations have been conducted in order to determine those configurations that produce the optimum results in terms of both heat transfer and pressure drop. The relevant geometric parameters involved in these experimental investigations are passage aspect ratio, AR [1, 2]; ridge angle of attack, α [3, 4]; pitch to height ratio, Pi/H [5–7]; blockage ratio, H/De [4, 7], and the manner by which ridges are positioned with respect to each other [8, 9]. Obviously, the above literature provides no information on the *effect of the ridge shapes* on the heat transfer and friction characteristics of the fully developed turbulent flows.

This paper basically describes the characteristics of the heat transfer and friction in channels where the various-shaped ridges are placed transversely to the streamwise direction on the two opposite walls. In this work, the same duct geometry and flow parameter as those adopted in Liou and Hwang [7] for the square-ridge case will be employed. The shapes of ridge investigated are triangular, semicircular, and square in cross section. A real-time holographic interferometer (LHI) is utilized to measure the local as well as average heat transfer coefficients. The research reported here is undertaken to fulfill the five objectives.

(1) To assess the possibility of hot-spots on the roughened walls by investigating the effect of ridge shapes on the distributions of local heat transfer coefficients of a ridged duct. The previous experimental [7, 10, 11] and numerical studies [12] indicated that for fully developed flows, the hot-spots exist in the recirculating region behind the square ridge because the fluid is nearly stagnant relative to the main stream in this region. It is interesting to know whether the channel with ridges of more streamlined shapes, such as semicircular and triangular ridges, can improve the heat transfer rate in this region.

(2) To provide a data base of detailed local heat transfer results for researchers and engineers to develop numerical models to predict the flow field and heat transfer characteristics in channels with various ridge shapes.

(3) To study the effect of the conductive and nonconductive ridges on the average heat transfer

† Author to whom all correspondence should be addressed.
Current address: Department of Mechanical Engineering, Chung-Hua Polytechnic Institute, Hsinchu, Taiwan 30067, R.O.C.

NOMENCLATURE

A	area of the ridged wall [m^2]
B	half channel height [m]
C	Gladstone–Dale constant
De	hydraulic diameter [m]
f	average friction factor
G	heat transfer roughness function
H	ridge height or radius [m]
H^+	roughness Reynolds number
k_f	air conductivity [W m^{-1} K^{-1}]
L_h	wetted length of the heated surface in one pitch [m]
L_r	wetted length of ridge surface [m]
$\dot{m}$	mass flow rate [kg s^{-1}]
Nu	local Nusselt number
$\overline{Nu}_o$	average Nusselt number for the smooth duct (at the same pumping power)
$\overline{Nu}_p$	average Nusselt number of the ridged wall (base on projective area)
$\overline{Nu}_t$	average Nusselt number of the ridged wall (based on total heat transfer area)
P	pressure [N m^{-2}]
Pi	ridge pitch [m]
Q	quantity of heat given to air from entrance to the considered cross section of the duct [W]
q''	local wall heat flux [W m^{-2}]
$\bar{q}''_r$	average wall heat flux of the ridge, i.e. $(\int_0^{L_r} q''\,dx)/L_r$ [W m^{-2}]
$\bar{q}_r$	ridge heat transfer [W]
$\bar{q}_t$	total heat transfer in one ridge pitch [W]
R	friction roughness function
Re	Reynolds number, $U \cdot De/\nu$
S	fringe order
St	Stanton number
T	local temperature of air [K]
T_m	bulk mean temperature of air [K]
T_w	wall temperature [K]
U	axial mean velocity [m s^{-1}]
W	half channel width [m]
X	axial coordinate (from ridge rear, Fig. 1)
X_h	axial coordinate (from duct entrance, Fig. 1)
Y	transverse coordinate
Z	spanwise coordinate.

Greek symbols

λ	wavelength of the laser beam
ρ	air density.

Subscripts

i	fringe index
r	reference
s	smooth channel
w	wall.

coefficient. In previous mass transfer studies [13, 14], metallic ridges without naphthalene coating were turbulence promoters. Note that metallic ridges without naphthalene coating on mass transfer surfaces are equivalent to insulated ridges on heat transfer surfaces. It is of importance to clarify the effect of ridge conductivity on the surface heat transfer coefficient.

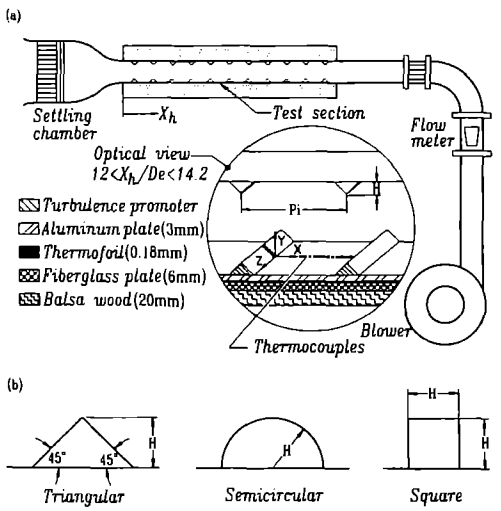

FIG. 1. Schematic diagram of the test apparatus and the construction of the test section.

(4) To quantify the performance of the three types of ridged ducts with respect to a corresponding smooth-walled duct. In order to take account of both heat transfer and pressure drop characteristics of the ridged ducts, the comparison will be made for the condition of constant pumping power.

(5) To develop heat transfer and friction correlations to account for the roughness parameters. The correlations can be used in the design of turbine blade cooling passages. The Reynolds number based on the hydraulic diameter and mean flow velocity is ranged from 7800 to 50000; the pitch-to-height (radius) ratio of the ridge element varies from 8 to 20; and the ridge height(radius)-to-channel hydraulic diameter ratio is fixed at 0.08.

EXPERIMENTAL APPARATUS AND CONDITIONS

Experimental apparatus

The schematic diagram of the channel flow loop and the test section is shown in Fig. 1(a). The flow system consists of a settling chamber, the test section,

a flow meter, and a centrifugal blower. The downstream end of the test section mates with a rectangular-to-circular transition piece which connects it to the air handling system.

The test section is 160 mm in width and 40 mm in height, i.e. a cross-sectional aspect ratio of 4 : 1. The length of the test section is 1200 mm. The shapes and sizes of the cascade promoters used in the experiment, as shown in Fig. 1(b), are an isosceles triangle (45 – 90 –45°) of 5.2 mm in height, a half-circle of 5.2 mm in radius, and a conventional square cross section with size of 5.2×5.2 mm^2. These ridges are glued periodically in line on the top and bottom surfaces of the channel in a required distribution. The ridge-angle of attack is 90°. A thin layer of thermally conducting epoxy cement (less than 0.13 mm in thickness) serves to ensure good contact between the plates and ridges. The thermal resistance of the thin layer of epoxy cement is negligible [7]. Both the plates and the promoters are made of aluminum. The aluminum plates are highly polished to minimize emissivity, hence radiation losses. The upper and lower walls of the test section each has one thermofoil; the thermofoil of 7.5 Ω is adhered uniformly between the aluminum plate and a fiberglass plate to ensure good contact. Each thermofoil can be independently controlled by a transformer and provides a controllable heat flux for the wall of the test section. The side walls of the entire test channel are made of plexiglass plates to provide optical access for interferometry measurements. Detailed construction of the test section is shown in Fig. 1.

Instrumentation

Real-time holographic interferometry is used to measure the temperature distribution of airflow in the ridged channel. The overall arrangement of holographic interferometer is illustrated in Fig. 2. A 3 W argon-ion (514.5 nm) laser (Spectra-Physic Model 2000) provides a coherent source in this work. After passing through a shutter, the laser beam is divided into two equal components by a beam splitter. One beam, the reference beam, bypasses the test section and is expanded by a 20× microscope objective and then filtered by a 10 μm diameter pinhole. The other beam, the object beam, is expanded and filtered by a 40× objective and a 10 μm pinhole and collimated by a 150 mm diameter, 500 mm focal length lens located 200 mm from the test section. The object beam then passes through the test section and is distorted as a result of the refractive index field generated by local temperature variation in the test section. The distorted object beam passes through the hologram, and is interfered with the comparison beam reconstructed by the reference beam. Thus an instantaneous interference field, of infinite-fringe setting, forms behind the hologram plate and indicates the instantaneous temperature field. A variable neutral density filter is used to adjust the intensity of the object beam. The photographic emulsion 8E56, made by Agfa-Gevaert Ltd, is found to be a suitable recording material for combining a good compromise between light sensitivity and resolution. The instantaneous interference field is digitized by a CCD camera which allows 512×512 pixel resolution with 256 grey levels per pixel and recorded on a VHS videocassette recorder for storage and further image processing.

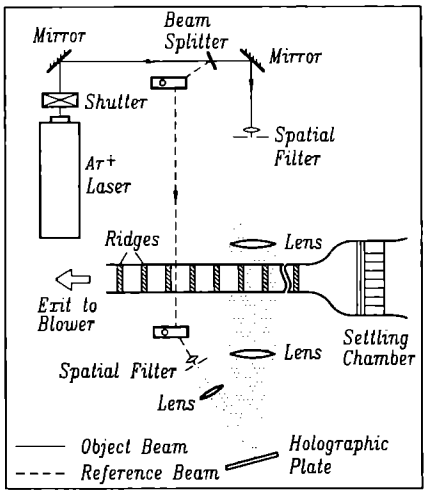

FIG. 2. Optical diagram of the laser holographic interferometer.

Copper–constantan thermocouples (of about 0.07 mm wire diameter) are used to measure the local wall temperature of the ridged surface. As shown in Fig. 1, 30 thermocouples are distributed along the spanwise centerline of the test section. To avoid the disturbance of the optical path and resolve the fluid-temperature distribution near the wall, the junction beads of the thermocouple (about 0.1 mm diameter) are cemented into small holes drilled into the back side of the plate approximately 1.0 mm from the front surface rather than attached to the wall directly. Therefore, the local wall temperature thus measured, may be averaged somehow by the conductive aluminum. For this reason, another test run is taken by directly attaching the thermocouple to the wall for the true wall temperature measurement at the same conditions without an optical process, and the results show that the maximum difference between the two methods is less than 1.5°C. A Yokogawa DA-2500 hybrid recorder and a PC-AT are used for temperature readings and recordings. Additionally, to measure pressure across the test duct, pressure taps are installed along the spanwise centerline of one of the ridged walls at 600 and 1100 mm, respectively, from the test duct entrance. A micro-differential transducer, Kyowa PDL-40B, is connected to these taps to measure the pressure. The measured pressure signal is subsequently amplified by a Kyowa WGA-200 A amplifier and is read from a digital readout. The pressure drop of present study is based on the adiabatic conditions.

Experimental conditions

The holograms are taken for the region between $X_h/De = 12$ and 14.2, where both hydrodynamic and thermal fully developed conditions are achieved [1, 15]. With uniform heat flux over the thermofoil, the wall heat flux may be expected to be uniform. However, due to the existence of the conducting wall and ridges, the heat input into the fluid is highly localized, and such an idealized circumstance of perfectly uniform wall heat flux is not obtained in the experiments. This can be demonstrated by the LHI measurements of local heat transfer rate, and will be shown later. In the interferometric experiments, the significant errors usually encountered are due to the end effect and the refraction effect [16]. The resulting errors in the fringe (temperature) shift due to the end and refraction effects are about 8 and 6%, respectively. The two-dimensionality of spanwise temperature profile of the flow field is checked by the thermocouple probing in this study, and the scatter in spanwise direction is less than 6% of the channel spanwise average temperature.

DATA REDUCTION

To analyze the interferogram, the equation of interferometry given by Hauf and Grigull [17] for a two-dimensional incompressible flow is used. This gives

$$S_i - S_{i-1} = 2T_r\rho_r CW(1/T_{S_i} - 1/T_{S_{i-1}})/\lambda, \quad (1)$$

where $S_i - S_{i-1}$ is the fringe shift, S_i the fringe order, C the Gladstone–Dale constant, and ρ_r the air density evaluated at reference temperature T_r. By setting $S_i - S_{i-1} = 1$, the temperature differences $T_{S_i} - T_{S_{i-1}}$ associated with each fringe are determined. Knowledge of at least one temperature and the temperature difference in the region of interest will provide the approximate heat transfer feature from wall to air.

By assuming that a thin layer of air is stationary next to the wall, and hence that the heat transfer in the region is by conduction only, the wall heat flux can be calculated from [7]

$$q'' = -k_f \cdot (\mathrm{d}T/\mathrm{d}Y)_w. \quad (2)$$

The wall-temperature gradient in the above equation is determined by a second-order curve fitting, based on a least-squares method, through the near wall values for temperature and fringe shift. Figure 3 shows the distributions of local wall heat flux ratio $(q''/\bar{q}'')$ and local wall temperature around the semicircular ridge. The former is calculated from the above equation and the latter is measured by thermocouple. It is obvious that the thermal boundary condition employed in this work is neither isothermal nor isoflux. Nevertheless, the local Nusselt number may be expressed in terms of both the measured temperature gradient at the surface and the measured surface temperature

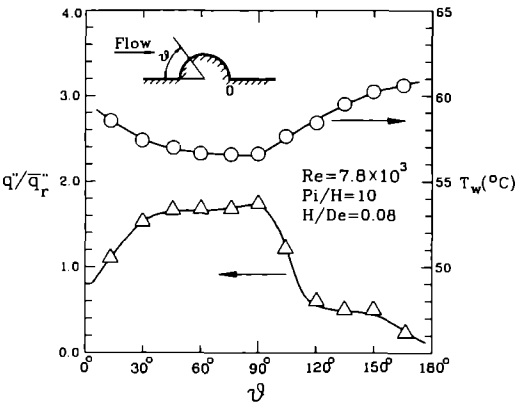

FIG. 3. Local wall heat flux and temperature distributions around the semicircular ridges.

$$Nu = q'' \cdot De/[(T_w - T_m) \cdot k_f] = -(\mathrm{d}T/\mathrm{d}Y)_w \cdot De/(T_w - T_m) \quad (3)$$

where T_w, the local wall temperature of the heated plate and ridges, is read from the output of the thermocouple. The local bulk mean air temperature T_m is calculated from an energy balance, and is defined as $T_m = T_{in} + Q/(\dot{m}c_p)$. The maximum uncertainty of the local Nusselt number is estimated to be less than 6.5% by the uncertainty estimation method of Kline and McClintock [18]. The Nu thus obtained is in contrast to those derived in the conventional experiments of stainless-foil heating [1] and naphthalene sublimation [5] methods. The local heat transfer coefficient obtained in the stainless-foil heating method is based on the constant heat flux boundary condition (CHF) and the measured surface temperature; whereas in the naphthalene sublimation method the local heat (mass) transfer coefficient is based on the constant wall temperature boundary condition (CWT) and the measured heat (mass) transfer rate.

The average Nusselt number $\overline{Nu}_t$ based on the total heat transfer area and average bulk mean temperature for the fully developed region is evaluated by the following equation

$$\overline{Nu}_t = \left[\int_0^{L_h} (\mathrm{d}T/\mathrm{d}Y)_w \, \mathrm{d}X\right] \cdot De/[L_h \cdot (\bar{T}_w - \bar{T}_m)] \quad (4)$$

where L_h is the wetted length of heated surface in one ridge pitch. $\bar{T}_w$ is the average wall temperature in one pitch, and the average bulk mean air temperature $\bar{T}_m$ is evaluated as

$$\left(\int_0^{L_h} T_m \, \mathrm{d}X\right) \Big/ L_h.$$

The $\overline{Nu}_t$ is estimated to have an uncertainty less than 9.6%.

The friction factors in the fully developed region of the duct may be expressed as

$$f = [(-\Delta P/\Delta X) \cdot De/4]/(\rho \cdot U^2/2). \quad (5)$$

In this expression, $\Delta P/\Delta X$ is an axial pressure gradient, which is evaluated by taking the ratio of the pressure difference and the distance of two consecutive pressure taps. The maximum uncertainty of f is estimated to be less than 7.3%.

RESULTS AND DISCUSSION

Isotherm patterns and local heat transfer

Typical examples of real-time interferograms taken from the full fields of temperature distributions of triangular-ridged, semicircular-ridged and square-ridged geometries are shown in Figs. 4(a)–(c) for $H/De = 0.08$, $Re = 13\,000$, and $Pi/H = 10$. The mean flow direction is from left to right. Figures 4(d) and (e) show the temperature contours near the triangular ridges for two different Reynolds numbers $Re = 7800$ and 18 000. It can be observed from these two figures that the thermal boundary layer on the upstream face of the triangular-ridge surface is very thin, and it increases with a decrease in Reynolds number. This indicates that the surface heat flux is very high in this region, and it increases with the increase of the flow rate. Similar trends can also be found for semicircular and square ridges.

A comparison of the distributions of local heat transfer coefficient of the three types of ridge shape employed is shown in Fig. 5. The results are expressed

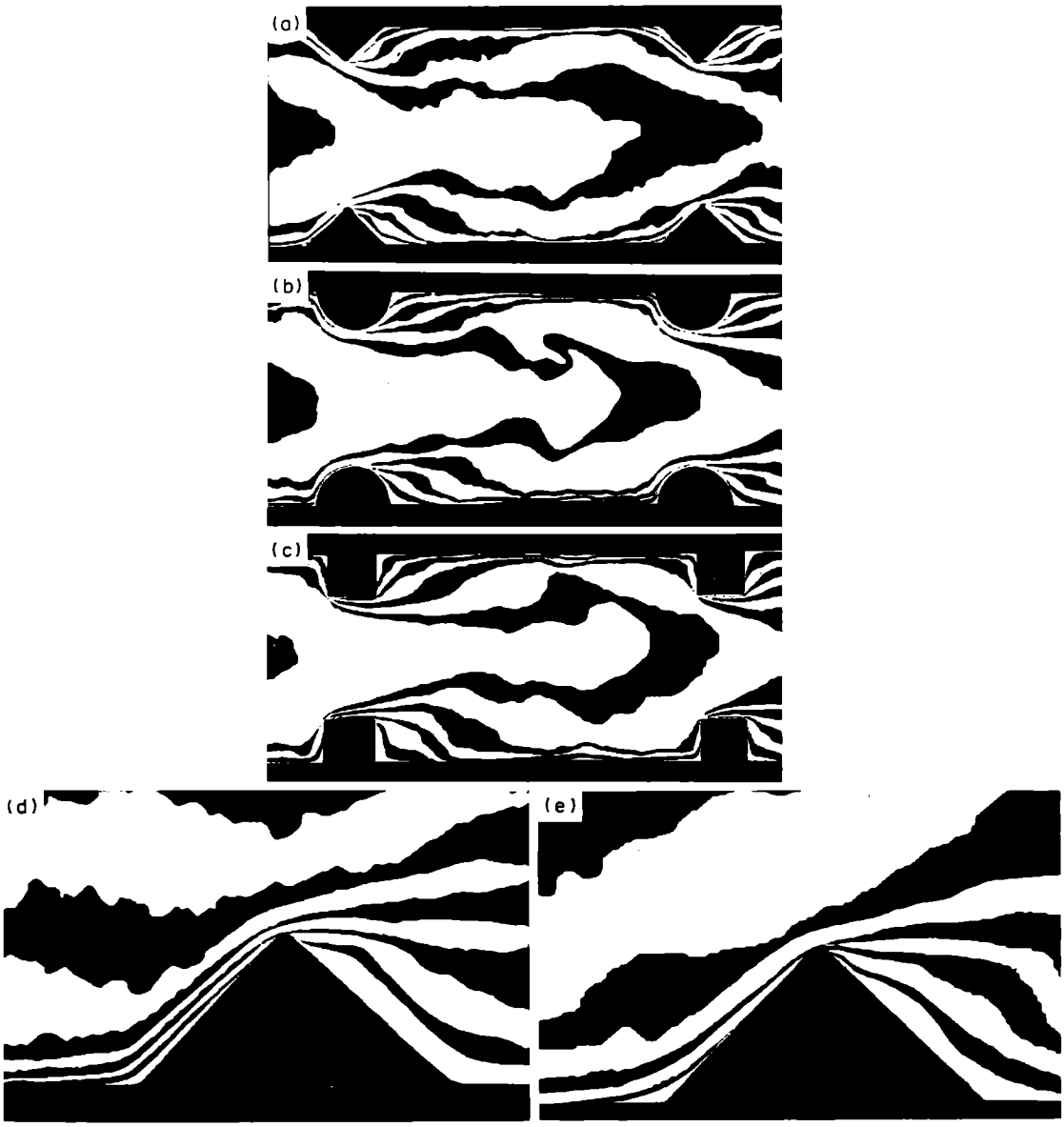

FIG. 4. Typical examples of the holographic interferograms: (a) $Re = 13\,000$, $Pi/H = 10$, and $H/De = 0.08$ (triangular ridge, full field); (b) $Re = 13\,000$, $Pi/H = 10$, and $H/De = 0.08$ (semicircular ridge, full field); (c) $Re = 13\,000$, $Pi/H = 10$, and $H/De = 0.08$ (square ridge, full field); (d) $Re = 7800$, $Pi/H = 10$, and $H/De = 0.08$ (triangular ridge, magnification); (e) $Re = 18\,000$, $Pi/H = 10$, and $H/De = 0.08$ (triangular ridge, magnification).

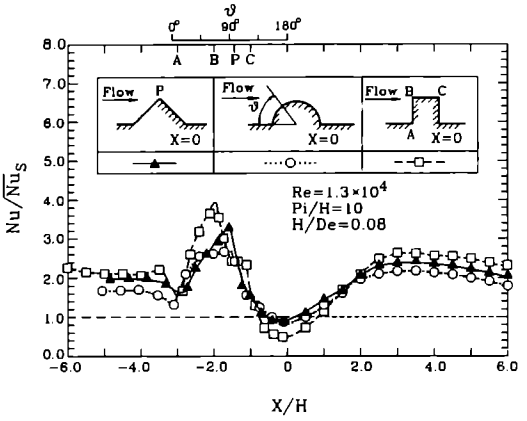

FIG. 5. Local Nusselt number distributions along the triangular-, semicircular- and square-ridged surfaces.

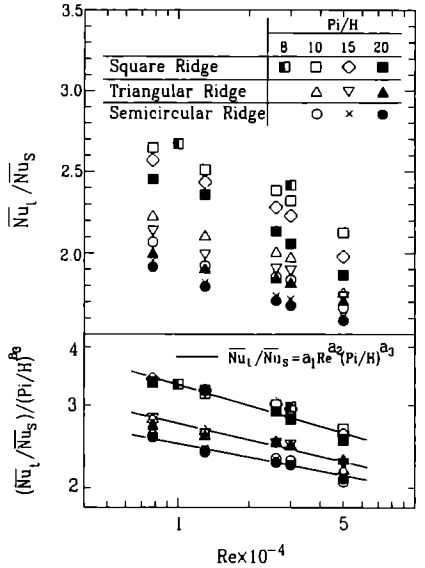

FIG. 6. Average Nusselt number vs Reynolds number.

in terms of the Nusselt number ratio, which is normalized by the well-known Dittus–Boelter correlation for fully developed turbulent flow in smooth circular tubes. Because of the use of the participating ridge, this figure displays the results not only between ridges but also of ridges themselves. The Nusselt number ratio distribution of the square-ridged wall has been investigated and described extensively [7] and is therefore not elaborated on in this paper. As for the triangular-ridged wall, the Nusselt number ratio increases fairly rapidly along the upstream ridge face. A local maximum of Nusselt number ratio appears near the ridge tip (P) where the flow is separated and the isotherms are packed (Fig. 4). Subsequently, the Nusselt number ratio decreases along the rear face of the ridge. This fact can be easily observable by the broad and widely spaced fringes (Fig. 4) at the rear of the ridge. Then the $Nu/\overline{Nu}_s$ increases along the duct wall and up to another local maximum, although not significantly, around the reattachment region in the inter-ridge region because of the combined effects of flow impingement and high turbulence transport [7]. Finally, the value of $Nu/\overline{Nu}_s$ decreases again gradually until it reaches the next ridge. With regard to the semicircular-ridged wall, the distribution of the $Nu/\overline{Nu}_s$ has a similar trend as that of the triangular-ridged wall, especially in the inter-ridge region.

As can be seen from Fig. 5, the semicircular-ridged case has the most uniform $Nu/\overline{Nu}_s$ distribution along the periphery of the ridge and duct wall for the three ridged walls investigated. The substantially low values of local Nusselt number ratio around the concave corner behind the square ridge is much more likely to occur than those behind the semicircular and triangular ridges. The maximum local heat transfer coefficients obtained for all of the three types of ridged surfaces are just at the points of flow separation.

Average Nusselt number

Figure 6(a) gives the average values of Nusselt number ratio of the three types of ridged walls as a function of Reynolds number. The plotted symbols indicate the actual results of the experiment. It is obvious from this figure that the heat transfer enhancement ($\overline{Nu}_t/\overline{Nu}_s > 1$) is attained in all of the ridge shapes employed. The increments of the average heat transfer coefficients are about 60–110, 70–120 and 90–170% for the semicircular-ridged, the triangular-ridged and the square-ridged walls as compared with the smooth-duct results, respectively, for the range of the investigated Reynolds number. With the data shown in Fig. 6(a), the $\overline{Nu}_t$ is well correlated in terms of the Re and the Pi/H. As shown in Fig. 6(b), the solid lines passing through these symbols are least-squares fits and can be expressed as the following equation:

$$\overline{Nu}_t/\overline{Nu}_s = a_1 \cdot Re^{a_2} \cdot (Pi/H)^{a_3} \qquad (6)$$

where the constants a_1, a_2 and a_3 are listed in Table 1. The maximum scatters of the data points relative to the least-squares lines are ± 3, ± 4, and $\pm 2.5\%$, respectively, for the semicircular-, the triangular-, and the square-ridged walls. For a fixed Reynolds number (flow rate) and a fixed pitch ratio, the square-ridged wall has the highest average heat transfer coefficient and the semicircular-ridged wall has the lowest one among the three ridged walls investigated. The correlation also shows that for the range of Pi/H investigated, more closely spaced ridge elements (smaller Pi/H) give rise to higher Nusselt number ratio regardless of the ridge shapes employed. The reason is provided below. First, the reattachment length (or the local $(Nu/\overline{Nu}_s)_{max}$, Fig. 5) behind the ridge alters slightly with the ridge shape as $Pi/H \geqslant 10$ (Fig. 5). Second, for larger ridge spacings, the redeveloping flow beginning at the reattachment point has a larger distance to develop into a thicker boundary layer

Table 1. Constants in equations (6) and (7)

	a_1	a_2	a_3	b_1	b_2	b_3
Semicircular ridge	6.786	−0.108	−0.121	0.581	−0.133	−0.601
Triangular ridge	8.381	−0.125	−0.121	0.590	−0.119	−0.579
Square ridge	11.752	−0.137	−0.121	0.684	−0.109	−0.606

before the succeeding ridge is encountered, hence reduced average heat transfer. Moreover, the semicircular ridged geometry has a more modest effect of Reynolds number on Nusselt number ratio than the square-ridged and triangular-ridged geometries. That is, the Reynolds number dependence (equation (6)) of the Nusselt number ratio of the semicircular-ridged wall is less than those of the other two. This is because in the semicircular-ridge case, the least mean-flow energy used for convection heat transfer is transferred into turbulent kinetic energy, which subsequently enhances the heat transfer rate through enhanced turbulent transport. The close correlation between the local Nusselt number and turbulent kinetic energy distributions has been demonstrated in Liou and Hwang [7] for the square-ridge case.

Friction factor

Friction factors measured for the different ridged ducts are plotted in Fig. 7. The results cover a Reynolds number range from 10 000, limited by the sensitivity of the pressure transducer used in the present work, to 50 000. The solid lines appearing in the figure are least-squares correlations of the form:

$$f = b_1 \cdot Re^{b_2} \cdot (Pi/H)^{b_3} \tag{7}$$

where the coefficients b_1, b_2 and b_3 are given in Table 1. The deviations in equation (7) from the test data are within ±3, ±2.5, and ±4%, respectively, for triangular-, semicircular-, and square-ridged ducts.

Although each of these ridge shapes has the same ridge height, the friction factors differ markedly. In comparison with the results of the smooth-duct flows (Blasius correlation), the extents of increase in f are approximate factors of 4–8, 5–10 and 7–15 for semicircular-ridged, triangular-ridged, and square-ridged duct flows, respectively. Obviously, the semicircular-ridged duct has the lowest level of friction factors. This is reasonable because the flow travels more smoothly over semicircular ridges than over square and triangular ridges. Moreover, the Reynolds number dependence of the friction factor of the square-ridged duct is slightly stronger than those of the semicircular-ridged duct and triangular-ridged duct. That is, the f–Re curve for the square-ridged duct is the flattest among the three ridged ducts. It is well established that the flatter the f–Re distribution is, the more significant are the inertial losses relative to the friction losses. Since the square cross-sectional blockage accentuates inertial losses, the flattest f–Re distribution is physically reasonable.

Comparison with mass transfer investigation

The ridge heat transfer ratio ($\bar{q}_r/\bar{q}_t$) is shown as a function of the Reynolds number in Fig. 8(a) for $H/De = 0.08$ and two different ridge pitch-to-height ratios $Pi/H = 8$ and $Pi/H = 10$. It can be seen from this figure that when the H/De is fixed, the ridge heat transfer ratio decreases with increasing Pi/H and does not significantly depend on the Reynolds number and the ridge shapes employed. Moreover, the $\bar{q}_r/\bar{q}_t$, typically above 31 and 25% (solid lines) for $Pi/H = 8$ and 10, respectively, is thus approximately comparable to the fraction that the ridge occupies in one-ridge–pitch wetted area. As a result, the average heat transfer rate of the ridge is almost the same as that of the duct wall. This observation can be further supported by

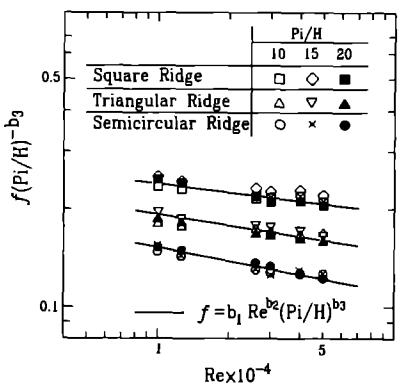

FIG. 7. Friction factor vs Reynolds number.

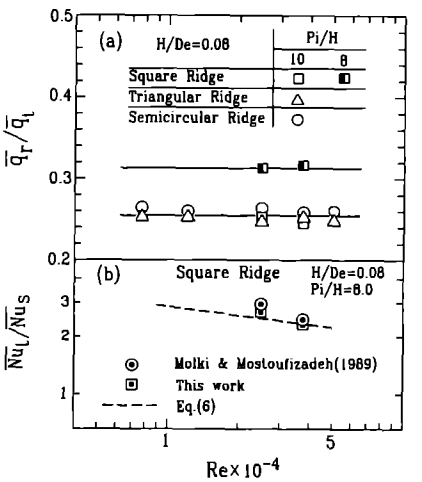

FIG. 8. (a) Ridge heat transfer ratio vs Reynolds number. (b) Comparison between the present study and the previous investigation.

the following comparison. In Fig. 8(b), the average ridged wall Nusselt number ratios of the fully developed channel flows for $\alpha = 90°$ are compared with the average ridged-wall mass transfer data of Molki and Mostoufizadeh [13]. Note that the previous study used the metallic ridges without naphthalene coating. Based on the heat and mass transfer analogy ($\overline{Nu}/\overline{Nu}_s = \overline{Sh}/\overline{Sh}_s$), the Sherwood number ratios are converted to Nusselt number ratios. As shown in this plot, it seems that the average heat transfer coefficients from the total heat transfer surfaces (inclusive of the heat transfer active ridge) are not significantly different from those from the smooth surfaces (exclusive of the heat transfer nonactive ridge). In the present heat transfer study, the heat transfer coefficients are based on total heat transfer area and total heat which is transferred both from the surfaces between the adjacent heat transfer ridges and from those on the ridges. In the previous mass transfer study [13], mass is transferred from the duct surfaces between the adjacent ridges only, and the area for the average mass transfer coefficient calculations is the original smooth surface area. Owing to the difference in the heat (mass) transfer surfaces over which the data are averaged in the two works, and the aforementioned comparable fractions of the total heat transfer area and the heat transfer rate those ridges occupy (Fig. 8(a)), the agreement between the present data and those of Molki and Mostoufizadeh [13] is reasonable. However, in real turbine cooling passages, the total heat is transferred not only from the duct surfaces between the adjacent ridges but also from the ridge surfaces themselves.

Performance analysis

The performance evaluation is usually accomplished by comparing heat transfer coefficients for channels with and without ridges per unit pumping power. Pumping power is proportional to $f \cdot Re^3$. Hence in Fig. 9, the performance is shown by the ratio of average Nusselt number ($\overline{Nu}_p$) and the value of smooth channel $\overline{Nu}_o$ at the same $f^{1/3} \cdot Re$. Note that the $\overline{Nu}_p$ is based on the projected area of a corresponding ridgeless wall. The reason for the use of $\overline{Nu}_p$ is that it can reflect the combined effects of the increased area provided by the ridge and the enhanced turbulence by distortion of velocity and temperature profiles caused by the existence of ridges [12]. As can be seen from this figure, the influence of the ridge shapes investigated on the thermal performance is not significant for constant pumping power. The ratio of the enhanced heat transfer to the increased friction factor decreases with increasing Reynolds number. That is, for the range of investigated Reynolds numbers the improvement in Nusselt number ratio of the ridged duct is more pronounced at lower Reynolds number, regardless of the ridge shapes employed.

Friction and heat transfer correlations

Analytical methods predicting the friction and the heat transfer coefficients in channels with various shaped ridges are not available because of the complex flow field created by ridge turbulators. Therefore, heat transfer designers still rely on semi-empirical correlations over a range of ridge configuration and flow Reynolds number of the heat transfer and the pressure drop calculations. Based on the ridged channel analysis discussed earlier [1], the wall similarity laws are employed to correlate the friction and heat transfer data for fully developed turbulent flow in a rectangular channel with two opposite ridged walls of the present study. The so-called friction and heat transfer roughness functions can be written as

$$R(H^+) = (f/2)^{-1/2} + 2.5 \cdot \ln\{(2H/De) \cdot [2W/(W+B)]\} + 2.5 \quad (8)$$

$$G(H^+, Pr) = R(H^+) + [f/(2\overline{St}) - 1]/(f/2)^{1/2} \quad (9)$$

where

$$H^+ = (H/De) \cdot Re \cdot (f/2)^{1/2}. \quad (10)$$

Figure 10 shows the friction roughness function

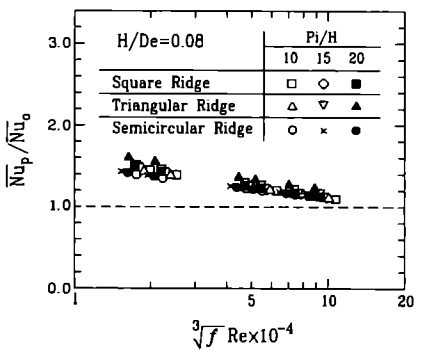

FIG. 9. Performance comparison of the triangular-, semicircular- and square-ridged duct flows.

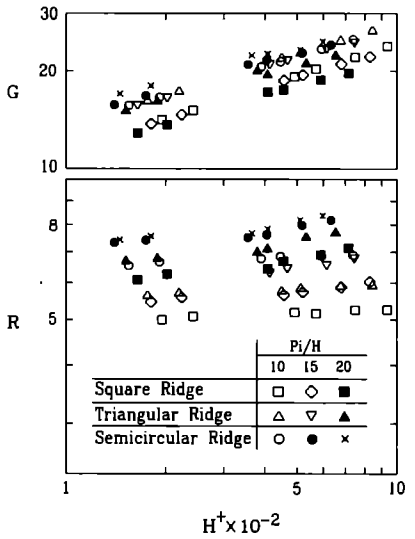

FIG. 10. Friction and heat transfer correlations of various shaped ridges.

Table 2. Constants in correlations (11) and (12)

	$R = c_1(Pi/H)^{c_2}(H^+)^{c_3}$			$G = d_1(Pi/H)^{d_2}(H^+)^{d_3}$		
	c_1	c_2	c_3	d_1	d_2	d_3
Semicircular ridge	2.398	0.261	0.073	5.068	−0.091	0.273
Triangular ridge	1.751	0.341	0.066	4.242	−0.082	0.299
Square ridge	1.535	0.364	0.059	3.322	−0.093	0.318

and the heat transfer roughness function vs roughness Reynolds number, respectively, for semicircular, triangular, and square ridges for a range of studied Reynolds number. The friction roughness and the heat transfer roughness data shown in Fig. 10 can be correlated as the following equations:

$$R = c_1 \cdot (Pi/H)^{c_2} \cdot (H^+)^{c_3} \quad (11)$$

$$G = d_1 \cdot (Pi/H)^{d_2} \cdot (H^+)^{d_3}. \quad (12)$$

The values of the coefficients and exponents, which are based on the least-squares curve fit lines through the various sets of data, are listed in Table 2. The maximum deviations of equations (11) and (12) are ± 8 and $\pm 9\%$, respectively. The semiconductor ridge has the highest friction roughness function, which implied the lowest pressure drop when compared to other ridge configurations. It can also be seen from Fig. 10 that the friction roughness function is almost independent of the roughness Reynolds number for all ridge shapes studied. As for the heat transfer roughness function, it increases with increasing roughness Reynolds number for all studied ridge shapes. The semicircular ridge has the highest G value, which means the lowest heat transfer. The slopes of G vs H^+ for semicircular and triangular ridges are slightly higher than the square ridge.

For a given ridge shape, ridge pitch, and flow Reynolds number, the friction factor could be predicted from the roughness function read from Table 2. Similarly, the heat transfer coefficient also can be predicted from both the heat transfer roughness function and friction roughness function, which are given in Table 2.

SUMMARY AND CONCLUSIONS

The fully developed turbulent heat transfer and friction in channels with two opposite walls roughened by triangular, semicircular and square ridges have been investigated experimentally by using LHI. New information of the distributions of the local heat transfer coefficient along the walls with various shaped ridges has been provided. The key conclusions are described as follows:

(1) For the range of Reynolds number studied, the presence of semicircular, triangular, and square ridges at two opposite walls yields about a 4–8 fold, a 5–10 fold, and a 7–15 fold increase in the average friction factors, respectively, relative to a smooth duct. The lowest friction factor is obtained in the semicircular-ridged case because of the most streamlined ridge shape for the ridged walls. Additionally, there are about a 1.6–2.1 fold, a 1.7–2.2 fold and a 1.9–2.7 fold increase in the average heat transfer coefficients as compared with the smooth-wall results for the semicircular-, triangular-, and square-ridged walls, respectively.

(2) The triangular-ridged, semicircular-ridged and square-ridged geometries have comparable thermal performances, but the square-ridged geometry is the most likely one to yield the hot spots around the concave corner behind the ridge among the three ridge geometries investigated.

(3) Although, in real turbine cooling passages, the total heat transfer rates are transferred from the ridges and from the surfaces between the adjacent ridges, the average heat (mass) transfer coefficients based on the total surface including the heat transfer active ridge surfaces, as in the present transfer study, are found to be not significantly different from those based on the smooth wall with heat transfer nonactive ridges, as in the previous mass transfer study.

(4) Semi-empirical correlations of the fully developed friction and heat transfer are developed for the channels with triangular, semicircular and square ridges.

Acknowledgement—Support for this work was provided by the National Science Council of the Republic of China under contract NSC 80-0401-E007-01.

REFERENCES

1. J. C. Han, Heat transfer and friction characteristics in rectangular channels with rib turbulators, *Trans. ASME J. Heat Transfer* **110**, 321–328 (1988).
2. J. C. Han, J. S. Park and C. K. Lei, Augmented heat transfer in rectangular channels of narrow aspect ratios with rib turbulators, *Int. J. Heat Mass Transfer* **32**, 1619–1630 (1989).
3. J. C. Han, J. S. Park and C. K. Lei, Heat transfer enhancement in channels with turbulence promoters, *Trans. ASME J. Engng Gas Turbines Pwr* **107**, 628–635 (1985).
4. J. C. Han and J. S. Park, Developing heat transfer in rectangular channels with rib turbulators, *Int. J. Heat Mass Transfer* **31**, 321–328 (1988).
5. E. M. Sparrow and W. Q. Tao, Symmetric vs asymmetric periodic disturbances at the walls of a heated flow passage, *Int. J. Heat Mass Transfer* **27**, 2133–2144 (1984).
6. J. C. Han, Heat transfer and friction in channels with two opposite rib-roughened walls, *Trans. ASME J. Heat Transfer* **106**, 774–782 (1984).

7. T. M. Liou and J. J. Hwang, Turbulent heat transfer augmentation and friction in periodic fully developed channel flows, *Trans. ASME J. Heat Transfer* **114**, 56–64 (1992).
8. D. E. Metzger, C. S. Fan and Y. Yu, Effects of rib angle and orientation on local heat transfer in square channels with angled roughness ribs. In *Compact Heat Exchangers, A Festschrift for A. L. London*. Hemisphere, Washington, DC (1990).
9. S. C. Lau, R. D. McMillin and J. C. Han, Turbulent heat transfer and friction in a square channel with discrete rib turbulators, *Trans. ASME J. Turbomachinery* **113**, 360–366 (1991).
10. J. F. Lockett and M. W. Collins, Holographic interferometry applied to rib-roughness heat transfer in turbulent flow, *Int. J. Heat Mass Transfer* **33**, 2439–2449 (1990).
11. T. M. Liou and J. J. Hwang, Developing heat transfer and friction in a ribbed rectangular duct with flow separation at inlet, *Trans. ASME J. Heat Transfer*, in press.
12. T. M. Liou, J. J. Hwang and S. H. Chen, Turbulent transport phenomena in channel with periodic rib turbulators, *AIAA J. Thermophysics*, in press.
13. M. Molki and A. R. Mostoufizadeh, Turbulent heat transfer in rectangular ducts with repeated-baffle blockages, *Int. J. Heat Mass Transfer* **32**, 1491–1499 (1989).
14. P. R. Chandra and J. C. Han, Pressure drop and mass transfer in two-pass ribbed channels, *AIAA J. Thermophysics* **3**, 315–320 (1989).
15. T. M. Liou and J. Lin, Measurements of turbulent flow in a duct with repeated ribs applied two opposite walls, *J. Chinese Inst. Engrs* **11**(4), 319–326 (1988).
16. R. J. Goldstein, Optical measurement of temperature. In *Measurements in Heat Transfer* (Edited by E. R. G. Eckert and R. J. Goldstein), 2nd Edn, pp. 241–294. Hemisphere, Washington, DC (1976).
17. W. Hauf and U. Grigull, Optical method in heat transfer. In *Advances in Heat Transfer* (Edited by J. P. Harttnett and T. F. Irvine, Jr.), Vol. 6, pp. 133–136. Academic Press, New York (1970).
18. S. J. Kline and F. A. McClintock, Describing uncertainties on single-sample experiments, *Mech. Engng* **57**, 3–8 (1953).